nature communications

Article

https://doi.org/10.1038/s41467-024-49229-6

Structural basis of promoter recognition by *Staphylococcus aureus* RNA polymerase

Received: 14 December 2023

Accepted: 28 May 2024

Published online: 06 June 2024

Check for updates

Linggang Yuan[1,5], Qingyang Liu[1,5], Liqiao Xu[1,5], Bing Wu[2,3] & Yu Feng[1,4]

Bacterial RNAP needs to form holoenzyme with σ factors to initiate transcription. While *Staphylococcus aureus* σ^A controls housekeeping functions, *S. aureus* σ^B regulates virulence, biofilm formation, persistence, cell internalization, membrane transport, and antimicrobial resistance. Besides the sequence difference, the spacers between the −35 element and −10 element of σ^B regulated promoters are shorter than those of σ^A regulated promoters. Therefore, how σ^B recognizes and initiates transcription from target promoters can not be inferred from that of the well studied σ. Here, we report the cryo-EM structures of *S. aureus* RNAP-promoter open complexes comprising σ^A and σ^B, respectively. Structural analyses, in combination with biochemical experiments, reveal the structural basis for the promoter specificity of *S. aureus* transcription. Although the −10 element of σ^A regulated promoters is recognized by domain $\sigma^A{}_2$ as single-stranded DNA, the −10 element of σ^B regulated promoters is co-recognized by domains $\sigma^B{}_2$ and $\sigma^B{}_3$ as double-stranded DNA, accounting for the short spacers of σ^B regulated promoters. *S. aureus* RNAP is a validated target of antibiotics, and our structures pave the way for rational drug design targeting *S. aureus* RNAP.

Bacterial RNA polymerase (RNAP) is the protein machinery responsible for transcription. Most bacterial RNAP is composed of five subunits-α^I, α^{II}, β, β′, and ω. The overall shape of bacterial RNAP resembles a crab claw, with the active center cleft located in the middle of two pincers[1]. During transcription initiation, the clamp, a mobile structural module that makes up much of one pincer, undergoes swing motions that open the active center cleft to allow entry of the promoter DNA[2–4]. During transcription elongation, the clamp closes up and secures the transcription bubble inside the active center cleft.

Bacterial RNAP forms holoenzyme with σ factors to initiate transcription[5]. Housekeeping σ factors (σ^{70} in *E. coli* and σ^A in other bacteria) govern the transcription of the majority of cellular genes. Housekeeping σ factors are comprised of several conserved domains: $\sigma_{1.1}$, $\sigma_{1.2}$, σ_2, σ_3, $\sigma_{3.2}$, and σ_4. For housekeeping σ factors, the consensus sequences of the promoter −35 element and −10 element are TTGACA and TATAAT, with an optimal spacer of 17 base pairs (bp). Extensive genetic, biochemical and structural studies demonstrate that $\sigma^{70/A}{}_4$ contacts the flap tip helix (FTH) of the RNAP β subunit and recognizes the promoter −35 element as double-stranded DNA (dsDNA), while $\sigma^{70/A}{}_2$ contacts the clamp helices of the RNAP β′ subunit and recognizes the promoter −10 element as single-stranded DNA (ssDNA)[6–10]. In contrast to the housekeeping σ factors, alternative σ factors direct RNAP to specialized operons in response to environmental and physiological cues. For example, *Mycobacterium tuberculosis* σ^H is a key regulator of the response to oxidative, nitrosative, and heat stresses[11]. For σ^H regulated promoters, the consensus sequences of the −35 element and −10 element are GGAACA and GTT, with an optimal spacer of 17 bp. Similar to the housekeeping σ factors, the −35 element and −10 element are recognized by $\sigma^H{}_4$ and $\sigma^H{}_2$ as dsDNA and ssDNA, respectively[12]. σ^{54}, which is involved in a range of different stress responses, has no sequence similarity to housekeeping σ factors at all.[13–17]. In contrast to σ^{70} and σ^H, σ^{54} is unable to unwind promoter DNA

[1]Department of Biophysics, and Department of Infectious Disease of Sir Run Run Shaw Hospital, Zhejiang University School of Medicine, Hangzhou, China. [2]Department of Gastroenterology and Hepatology, Minhang Hospital, Fudan University, Shanghai, China. [3]Institute of Fudan-Minhang Academic Health System, Minhang Hospital, Fudan University, Shanghai, China. [4]Key Laboratory for Diagnosis and Treatment of Physic-Chemical and Aging Injury Diseases of Zhejiang Province, Hangzhou, China. [5]These authors contributed equally: Linggang Yuan, Qingyang Liu, Liqiao Xu. e-mail: yufengjay@zju.edu.cn

https://doi.org/10.1038/s41467-024-49229-6

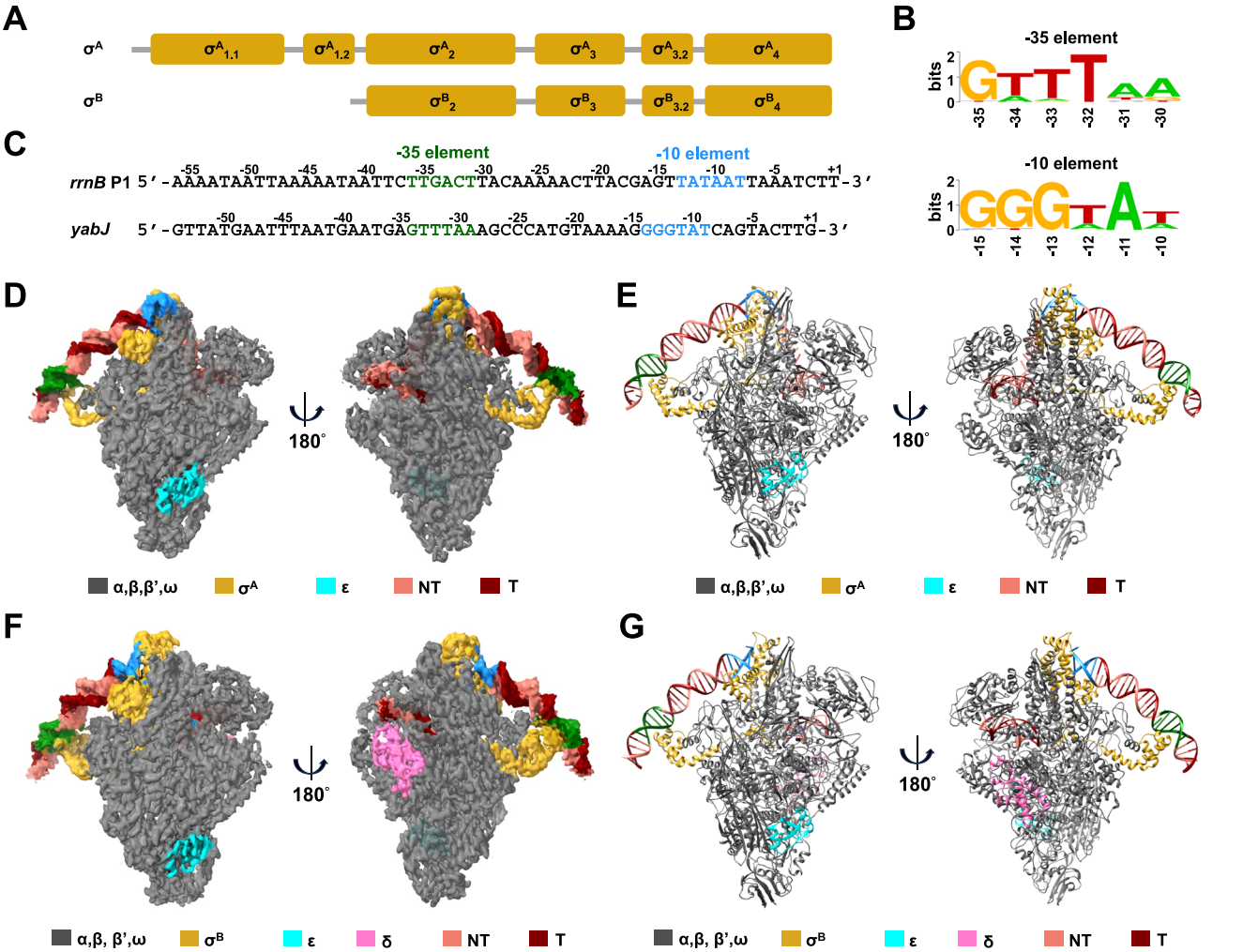

Fig. 1 | The cryo-EM structures of σ^A-RPo and σ^B-RPo. A Domain organization of *S. aureus* σ^A and σ^B. **B** The consensus sequences of *S. aureus* σ^B-dependent promoters. The sequence logo was created on the WebLogo website (http://weblogo.berkeley.edu) using an alignment of all the σ^B-dependent promoters listed in Supplementary Table 1. The height of the letters is proportional to their frequency. **C** Sequences of *S. aureus rrnB* P1 and *yabJ* promoters, which are recognized by σ^A and σ^B, respectively. Green, the −35 element; blue, the −10 element. **D**, **E** The electron potential map without B-factor sharpening (**D**) and the model (**E**) of σ^A-RPo. Gray, RNAP core except ε; cyan, ε; yellow, σ^A; salmon, nontemplate strand DNA; red, template strand DNA; green, the −35 element; blue, the −10 element. **F**, **G** The electron potential map without B-factor sharpening (**F**) and the model (**G**) of σ^B-RPo. Gray, RNAP core except ε and δ; cyan, ε; pink, δ; yellow, σ^B; salmon, nontemplate strand DNA; red, template strand DNA; green, the −35 element; blue, the −10 element.

spontaneously. Instead, it requires ATP dependent activator proteins bound upstream of the promoter in order to initiate transcription. The consensus sequences of the promoter −24 element and −12 element are TGGCACG and TTGCW (W = A/T), with an optimal spacer of 4 bp. σ^{54} recognizes the promoter −24 element and −12 element using RpoN and ELH-HTH domains, respectively.

σ^B was first discovered in *Bacillus subtilis*[18]. The activity of σ^B is tightly regulated by the Rsb proteins[19,20]. When there is no stress, RsbW binds to and sequesters σ^B. Under stress conditions, RsbV binds to RsbW and releases σ^B. Additionally, RsbU regulates the activity of σ^B by dephosphorylating RsbV. In *S. aureus*, σ^B is one of the major determinants of pathogenicity and virulence[21–23]. Although σ^A and σ^B share σ_2, σ_3, $\sigma_{3.2}$, and σ_4, the promoters of σ^B regulated genes show distinct signatures from those of σ^A regulated genes, ensuring the specificity of transcription regulation (Fig. 1A, B). First, the consensus sequence of the −35 element (GTTTWW) and −10 element (GGGWAW) are dramatically different from those of σ^A dependent promoters[21]. More importantly, the spacers between the −35 element and −10 element are divergent (~17 bp for σ^A *vs* ~ 14 bp for σ^B).

Despite four decades of study, we still do not know how σ^B recognizes its promoters specifically and turns on transcription efficiently. In this work, we solved the cryo-EM structures of *S. aureus* RNAP-promoter open complex comprising σ^A and σ^B (σ^A-RPo and σ^B-RPo), respectively. The structures define the interactions between RNAP holoenzyme and DNA, thus explaining the promoter specificity as well as the stabilization of transcription bubble.

Results

To obtain *S. aureus* RNAP for structural study, we cloned genes encoding *S. aureus* RNAP α, β, β′, ω, δ, and ε subunits into the pET21a vector and expressed the recombinant RNAP core enzyme in *E. coli* (Supplementary Fig. 1A, B). The activity of the RNAP core enzyme was verified using a primer extension assay on an RNA-DNA scaffold (Supplementary Fig. 1C). Then the RNAP holoenzyme was prepared by mixing the RNAP core enzyme with an excess of a σ factor and purified by size exclusion chromatography. In vitro transcription experiments confirmed that σ^A-RNAP holoenzyme is active in transcribing from the *S. aureus rrnB* P1 promoter, a typical σ^A dependent promoter, and that σ^B-RNAP holoenzyme is efficient in transcribing from the *S. aureus yabJ* promoter[21], a verified σ^B dependent promoter (Supplementary Fig. 1D).

To obtain the structure of σ^A-RPo, we used a DNA scaffold modified from *S. aureus rrnB* P1 promoter, which contains a consensus −35

element and a consensus −10 element (Fig. 1C). To obtain the structure of σ^B-RPo, we used a DNA scaffold modified from *S. aureus yabJ* promoter. The scaffold contains a consensus −35 element and a consensus −10 element, as well. The formation of RPo was confirmed by electrophoretic mobility shift assay (EMSA, Supplementary Fig. 2). The structures of σ^A-RPo and σ^B-RPo were determined at 3.7 Å and 3.3 Å by cryo-EM single particle reconstruction, respectively (Supplementary Figs. 3–6 and Supplementary Table 2). The cryo-EM maps show unambiguous densities for α, β, β′, ω, δ, ε, σ, and the DNA scaffolds (Fig. 1 and Supplementary Fig. 7). The overall structure of *S. aureus* RNAP resembles those from other species with an overall shape of crab craw[1,24–29]. The clamp adopts a closed conformation, securing the transcription bubble and downstream dsDNA in the main channel (Supplementary Fig. 8).

There is only one insertion in *S. aureus* RNAP (βIn5, L281-K373, Supplementary Fig. 9). βIn5 inserts into and packs against the β lobe, resulting in an interface area of 1617 Å^2. The large interface area makes βIn5 and β lobe look like one whole domain. Since β lobe is the target of transcription factors[30–32], βIn5 may serve as the docking site for transcription factors. In *E. coli* RNAP, βSI1 inserts into the β lobe at a different site. The interface area of βSI1 is much smaller and it is attached to the β lobe loosely.

δ and ε are subunits specific to the *Firmicutes*. Although the density for δ subunit is weak in σ^A-RPo, it is strong in σ^B-RPo (Fig. 1D, F). In agreement with the cryo-EM structures of *Bacillus subtilis*[28,29], the N-terminal domain of δ binds between the β′ subunit shelf and jaw, while the C-terminal region is disordered. Because the C-terminal region is rich in acidic residues, it may prevent the nonspecific interaction between RNAP and DNA[33,34]. The ε subunit is positioned in a cavity formed by the α subunit N-terminal domains, β subunit and β′ subunit, stabilizing the multi-subunit complex.

In the structure of σ^B-RPo, $\sigma^B{}_4$ clamps the β subunit flap domain tip helix (FTH) and mediates sequence-specific interactions with the promoter −35 element in the same way as $\sigma^A{}_4$ (Fig. 2A and Supplementary Fig. 10). In particular, σ^B residue R241 is positioned to make a hydrogen bond with the O6 of −35G. The hydroxyl group of σ^B residue S235 forms a van der Waals interaction with the C5-methyl group of −34T. σ^B residue M237 makes a van der Waals interaction with N7 of the A opposite −33T. σ^B residue Q236 is positioned to make a hydrogen bond with N6 of the A opposite −32T. Moreover, there is a potential electrostatic interaction between σ^B residue R244 and DNA backbone phosphate group. Alanine substitution of these residues does not affect RNAP holoenzyme formation (Supplementary Fig. 11), but hampers σ^B dependent RPo formation and transcription activity (Fig. 2B, C), confirming that the cryo-EM structure is biologically relevant. In accordance, mutation of the interacting nucleotides impairs σ^B dependent RPo formation and transcription activity, as well (Fig. 2D, E). Sequence alignment indicates that these residues are divergent between σ^A and σ^B (Fig. 2F), explaining the specificity of σ^B mediated transcription regulation.

In the structure of σ^A-RPo, $\sigma^A{}_2$ contacts the clamp helices and mediates sequence specific interactions with the promoter −10 element (Fig. 3A). Specifically, $\sigma^A{}_2$ interacts with the first position of the −10 element as dsDNA and the second through sixth positions of the −10 element as ssDNA. σ^A residue W189 stacks on the base of −12T, forming a wedge that forces the base of −11A to unstack and flip outside the DNA helix, where it is captured by binding within a pocket formed by σ^A residues F175, K179, F181, and Y186. −7T is flipped out of the base stack and buried deeply in a cognate pocket, as well. In addition, $\sigma^A{}_{1.2}$ interacts with nontemplate-strand ssDNA extensively, stabilizing the transcription bubble. Especially, residue L111 makes up one wall of the −7T pocket. These interactions are reminiscent of the interaction observed in the crystal structure of *Thermus aquaticus* $\sigma^A{}_2$ in complex with −10 element ssDNA[6].

The most striking feature of σ^B-RPo is that the upstream 4-bp of the −10 element is co-recognized by $\sigma^B{}_2$ and $\sigma^B{}_3$ as dsDNA (Fig. 3B). The last α helix of $\sigma^B{}_2$ and the first α helix of $\sigma^B{}_3$ bind in the DNA major groove and make sequence specific interactions with the upstream 3 bp of the promoter −10 element. Particularly, σ^B residues R110 and R100 are positioned to form hydrogen bonds with O6 of −15G and −14G, respectively. $\sigma^B{}_2$ residue R97 is placed to make a van der Waals interaction with N7 of −13G. Strikingly, the fifth bp is unwound and the base of −11A inserts into a hydrophobic pocket formed by σ^B residues F79 and F86. In addition, σ^B residue R74 is positioned to form salt bridges with DNA backbone phosphate groups. Alanine substitution of these residues does not affect RNAP holoenzyme formation (Supplementary Fig. 11), but compromises σ^B dependent RPo formation and transcription activity significantly (Fig. 3C, D), verifying their importance. Consistently, mutation of the interacting nucleotides impairs σ^B dependent RPo formation and transcription activity, as well (Fig. 3E, F). Again, these residues are divergent between σ^A and σ^B (Fig. 3G), explaining the specificity of σ^B mediated transcription regulation. Although $\sigma^A{}_{1.2}$ interacts with nontemplate-strand ssDNA extensively in σ^A-RPo, the density of the nontemplate-strand ssDNA in σ^B-RPo is weak due to the lack of $\sigma^B{}_{1.2}$ (Supplementary Fig. 7B).

Previous studies showed that *E. coli* $\sigma^{70}{}_{1.1}$ modulates the DNA binding activity of σ^{70}. In the absence of RNAP, $\sigma^{70}{}_{1.1}$ inhibits the DNA binding function of free σ^{70} [35]. In the presence of RNAP, $\sigma^{70}{}_{1.1}$ binds in the main channel of RNAP and prevents the nonspecific binding of DNA[36,37]. There is no density for *S. aureus* $\sigma^A{}_{1.1}$ in the structure of σ^A-RPo, but the structure of *S. aureus* $\sigma^A{}_{1.1}$ predicted by AlphaFold is very similar to the structure of *E. coli* $\sigma^{70}{}_{1.1}$[36] and *B. subtilis* $\sigma^A{}_{1.1}$[38], suggesting their similar roles (Fig. 4A). To delineate the function of *S. aureus* $\sigma^A{}_{1.1}$, we constructed and purified $\sigma^A{}_{1.1}$ truncated σ^A. Fluorescence polarization experiments demonstrate that $\sigma^A{}_{1.1}$ truncated σ^A binds promoter DNA better than the full-length σ^A (Fig. 4B). Moreover, truncation of $\sigma^A{}_{1.1}$ increases σ^A dependent RPo formation, confirming that the roles of *S. aureus* $\sigma^A{}_{1.1}$ and *E. coli* $\sigma^{70}{}_{1.1}$ are similar (Fig. 4C).

Discussion

Structural comparison of different σ factors reveals the reason for the short spacers between the −35 element and −10 element of σ^B regulated promoters. Similar to the structure of *E. coli* σ^{70}-RPo[10], the structure of *S. aureus* σ^A-RPo demonstrates that $\sigma^A{}_4$ recognizes the promoter −35 element through its helix-turn-helix (HTH) motif and $\sigma^A{}_2$ recognizes the promoter −10 element through two cognate protein pockets (Fig. 5A). Despite the lack of $\sigma_{1.1}$, $\sigma_{1.2}$, and σ_3, the structure of *M. tuberculosis* σ^H-RPo shows that σ^H also binds to the promoter in an analogous manner[12]. Like σ^{70}/σ^A and σ^H, $\sigma^B{}_4$ recognizes the promoter −35 element through its HTH motif. Unlike σ^{70}/σ^A and σ^H, $\sigma^B{}_2$ and $\sigma^B{}_3$ co-recognize the −10 element. Since σ_2, σ_3, and σ_4 are anchored to RNAP surface at the fixed locations, the spacers between the −35 element and −10 element of σ^B regulated promoters are ~3 bp shorter than those of σ^{70}/σ^A and σ^H regulated promoters.

The conversion from RNAP-promoter closed complex (RPc) to RPo has been studied extensively using *E. coli* σ^{70} [30,31,39]. In σ^{70}-RPc, sequence-specific recognition of the promoter −35 element by σ_4 positions the critical and conserved −11A of −10 element in line with σ_2 residues that later capture the flipped base to nucleate transcription bubble formation. In σ^{70}-RPo, two conserved pockets in σ^{70} capture the flipped bases of the −10 element (−11A and −7T) and stabilize the transcription bubble. *S. aureus* σ^A probably works in the same way as *E. coli* σ^{70}. As for σ^B, sequence-specific recognition of the promoter −35 element and −10 element by σ_4, σ_3, and σ_2 positions the conserved −11A of −10 element in line with σ_2 residues that later capture the flipped base to nucleate transcription bubble formation. Since there is no structural equivalent of the −7T pocket of σ^{70}/σ^A, only one base of the −10 element (−11A) is flipped and specifically captured in a protein pocket.

https://doi.org/10.1038/s41467-024-49229-6

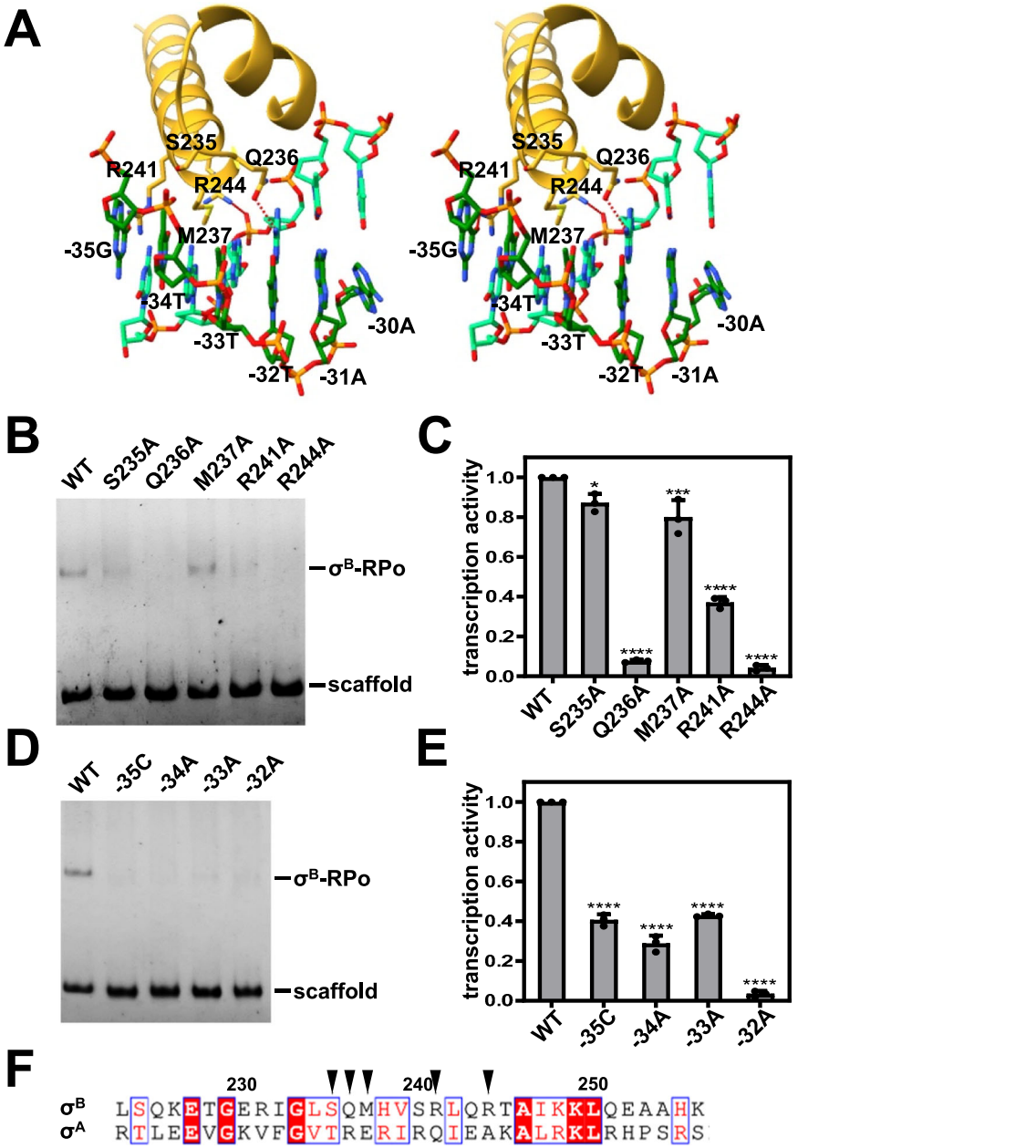

Fig. 2 | σ-DNA interactions responsible for −35 element recognition. A σ^B_4-DNA interactions are depicted in stereo view. Yellow, σ^B_4; dark green, nontemplate strand DNA; light green, template strand DNA. The potential hydrogen bonds are shown as dashed lines. **B** EMSA shows that the substitution of DNA interacting residues impairs σ^B-RPo formation. Source data are provided as a Source Data file. **C** Ribogreen transcription assay shows that the substitution of DNA interacting residues impairs σ^B dependent transcription. Error bars represent mean ± SD of $n = 3$ experiments. S235A, $p = 0.0252$; Q236A, $p < 0.0001$; M237A, $p = 0.0008$; R241A, $p < 0.0001$; R244A, $p < 0.0001$. One-way ANOVA. Source data are provided as a Source Data file. **D** EMSA shows that the mutation of the interacting nucleotides impairs σ^B-RPo formation. **E** Ribogreen transcription assay shows that the mutation of the interacting nucleotides impairs σ^B dependent transcription. Error bars represent mean ± SD of $n = 3$ experiments. −35C, $p < 0.0001$; −34A, $p < 0.0001$; −33A, $p < 0.0001$; −32A, $p < 0.0001$. One-way ANOVA. Source data are provided as a Source Data file. **F** Sequence alignment of *S. aureus* σ^A and σ^B. The DNA interacting residues of σ^B are indicated by black triangles. Source data are provided as a Source Data file.

σ^B orthologs are presented in many Gram-positive bacteria, such as *Bacillus subtilis*, *Bacillus cereus*, *Clostridium difficile*, *Listeria monocytogenes*, and *Mycobacterium tuberculosis* (σ^F, instead of σ^B, is a σ^B ortholog). Their regulated promoters all share similar consensus sequences and spacer lengths[21,40–44]. Sequence alignment indicates that the DNA interacting residues identified in this work are highly conserved among these σ^B orthologs (Fig. 5B), suggesting the finding of this work can be applied to other bacteria, as well.

Our cryo-EM structures also hints at mechanisms of action for δ subunit during transcription initiation. Our cryo-EM structures demonstrate that the N-terminal domain of δ subunit anchors the C-terminal region at the rim of the main channel, where the C-terminal region can reach into the main channel and exclude the binding of DNA (Supplementary Fig. 8). Accordingly, δ subunit has been shown to interfere with the interaction between DNA and RNAP[33,34]. Our biochemical experiments indicate that $\sigma^A_{1.1}$ also resides in the main channel and exclude the binding of DNA. Therefore, the C-terminal region of δ subunit probably competes with $\sigma^A_{1.1}$ and occupies similar regions in the main channel. Consistently, *Bacillus subtilis* δ subunit exhibits negative cooperativity

https://doi.org/10.1038/s41467-024-49229-6

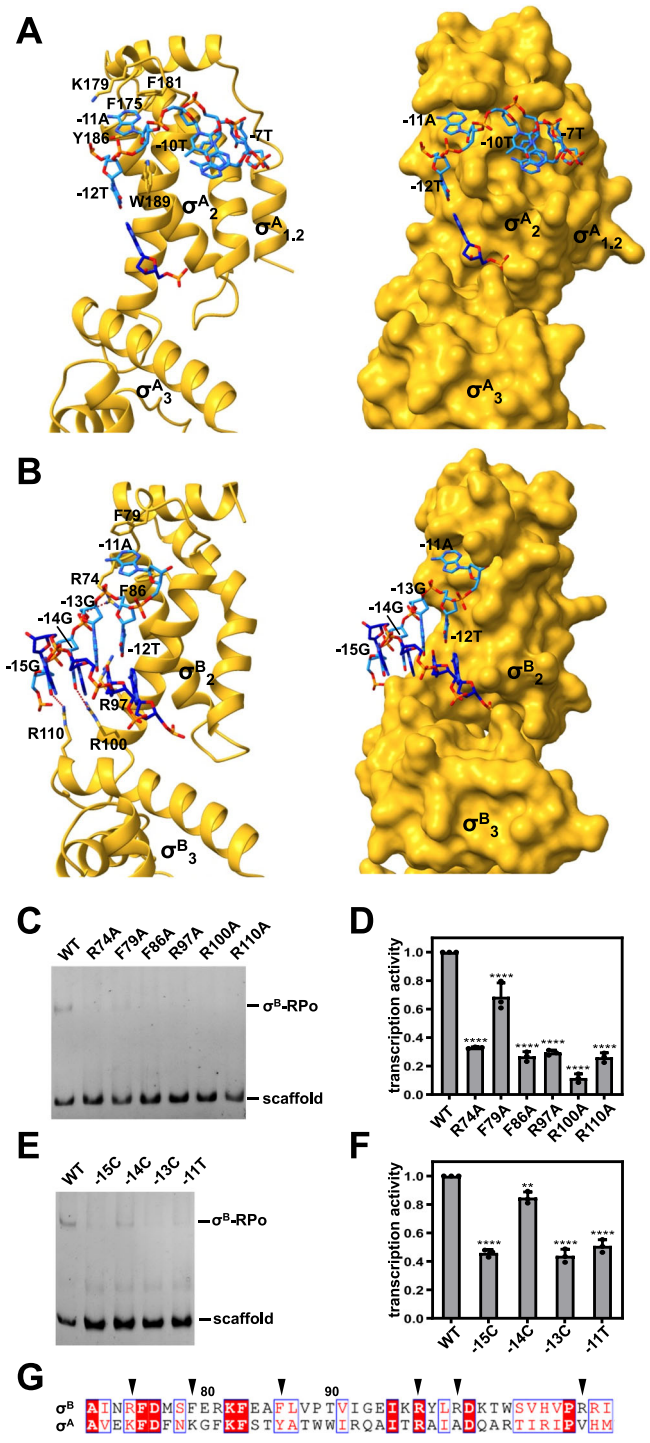

Fig. 3 | σ-DNA interactions responsible for −10 element recognition. A $\sigma^A{}_2$-DNA interactions. Yellow, σ; light blue, nontemplate strand DNA; dark blue, template strand DNA. Left subpanel, ribbon representation; right subpanel, surface representation. **B** $\sigma^B{}_2$ and $\sigma^B{}_3$ co-recognize the −10 element. Yellow, σ; light blue, nontemplate strand DNA; dark blue, template strand DNA. Left subpanel, ribbon representation; right subpanel, surface representation. **C** EMSA shows that the substitution of DNA interacting residues impairs σ^B-RPo formation. Source data are provided as a Source Data file. **D** Ribogreen transcription assay shows that the substitution of DNA interacting residues impairs σ^B dependent transcription. Error bars represent mean ± SD of $n = 3$ experiments. R74A, $p < 0.0001$; F79A, $p < 0.0001$; F86A, $p < 0.0001$; R97A, $p < 0.0001$; R100A, $p < 0.0001$; R110A, $p < 0.0001$. One-way ANOVA. Source data are provided as a Source Data file. **E** EMSA shows that the mutation of the interacting nucleotides impairs σ^B-RPo formation. **F** Ribogreen transcription assay shows that the mutation of the interacting nucleotides impairs σ^B dependent transcription. Error bars represent mean ± SD of $n = 3$ experiments. −15C, $p < 0.0001$; −14C, $p = 0.0030$; −13C, $p < 0.0001$; −11T, $p < 0.0001$. One-way ANOVA. Source data are provided as a Source Data file. **G** Sequence alignment of *S. aureus* σ^A and σ^B. The DNA interacting residues of σ^B are indicated by black triangles.

with σ^A and favors its exchange for alternative σ factors that lack $\sigma^A{}_{1.1}$[45–47].

RNAP inhibitor rifampin has been successful in treating *S. aureus* infection, especially periprosthetic joint infection[48]. However, the danger of rapid emergence of resistance restricts its usage[49]. Resistance to rifampin in *S. aureus* is determined by mutations in the gene encoding the RNAP β subunit. The structures presented here provide a structural basis for these resistant mutations. After we dock the rifampin into our structures (Supplementary Fig. 12), we find that all resistant mutations are positioned within 10 Å from rifampin. Some of them even directly contact rifampin. For example, substitution of β residue H481 would be expected to disrupt two hydrogen bonds between RNAP and rifampin.

Methods

Expression and purification of *S. aureus* RNAP core enzyme

Genes *rpoA*, *rpoB*, *rpoC*, *rpoZ*, *rpoE*, and *rpoY* were amplified from *S. aureus* strain N315 and subcloned into the pET21a vector by homologous recombination (Supplementary Data 1). 10 x histidine codons were placed after rpoC gene to facilitate purification. *S. aureus* RNAP core enzyme was prepared from *E. coli* strain BL21(DE3) (Invitrogen, Inc.) transformed with plasmid pET21a-Sau-rpoABCZEY. Single colonies of the resulting transformants were used to inoculate 100 mL LB broth containing 100 μg/mL ampicillin, and cultures were incubated 16 h at 37 °C with shaking. Aliquots (10 mL) were used to inoculate 1 L LB broth containing 100 μg/mL ampicillin, cultures were incubated at 37 °C with shaking until $OD_{600} = 0.6$, cultures were induced by addition of IPTG to 0.5 mM, and cultures were incubated 15 h at 20 °C. Then cells were harvested by centrifugation (5000×*g*; 15 min at 4 °C), resuspended in 30 mL lysis buffer (20 mM Tris-HCl, pH 8.0, 0.5 M NaCl, 2 mM EDTA, 5% glycerol, and 5 mM DTT) and lysed using a JN-02C cell disrupter (JNBIO, Inc.). After poly(ethyleneimine) precipitation and ammonium sulfate precipitation, the pellet was resuspended in buffer A (20 mM Tris-HCl, pH 8.0, 0.5 M NaCl, and 5% glycerol) and loaded onto a 5 mL column of Ni-NTA agarose (Qiagen, Inc.) equilibrated with buffer A. The column was washed with 25 mL buffer A containing 20 mM imidazole and eluted with 25 mL buffer A containing 0.3 M imidazole. The eluate was further purified by anion-exchange chromatography on a HiTrap Q HP column (GE Healthcare, Inc.). Fractions containing *S. aureus* RNAP core enzyme were applied to a HiLoad 16/600 Superdex 200 column (GE Healthcare, Inc.) equilibrated in 10 mM HEPES, pH 7.5, and 100 mM KCl, and the column was eluted with 120 mL of the same buffer. Fractions containing *E. coli* RNAP core enzyme were stored at −80 °C. Yield was ~0.6 mg/L.

Expression and purification of *S. aureus* σ^A and σ^B

Genes encoding *S. aureus* σ^A and σ^B were amplified from *S. aureus* strain N315 and subcloned into pET21a vector. *S. aureus* σ^A and σ^B were prepared from *E. coli* strain BL21(DE3) (Invitrogen, Inc.) transformed with plasmids pET21a-σ^A and pET21a-σ^B, respectively. Single colonies of the resulting transformants were used to inoculate 1L LB broth containing 100 μg/mL ampicillin, cultures were incubated at 37 °C with shaking until OD_{600} = 0.6, cultures were induced by addition of IPTG to 0.5 mM, and cultures were incubated 15 h at 20 °C. Then cells were harvested by centrifugation (5000×*g*; 15 min at 4 °C), resuspended in 30 mL buffer B (20 mM Tris-HCl, pH 8.0, 0.5 M NaCl) and lysed using a JN-02C cell disrupter (JNBIO, Inc.). The lysate was centrifuged (20,000×*g*; 45 min at 4 °C), and the supernatant was loaded onto a 5 mL column of Ni-NTA agarose (Qiagen, Inc.) equilibrated with

https://doi.org/10.1038/s41467-024-49229-6

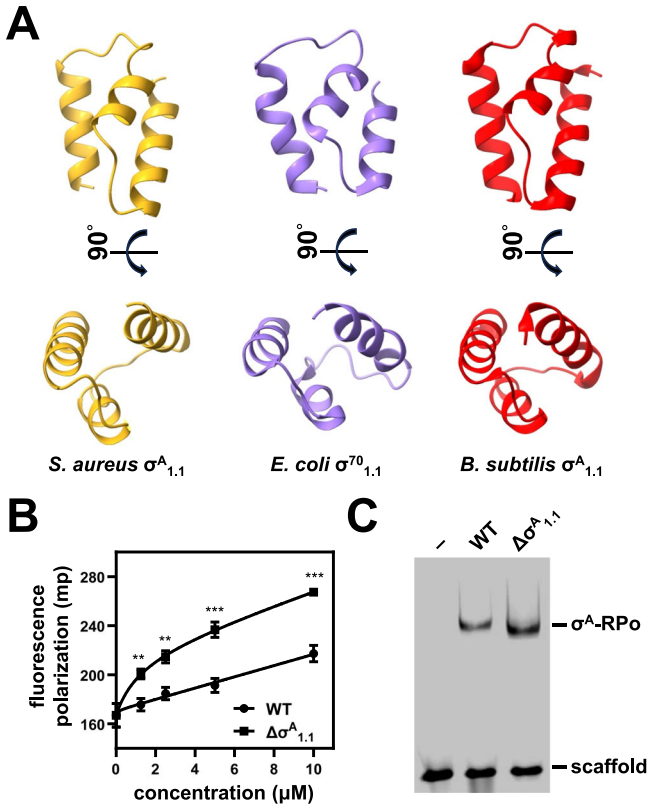

Fig. 4 | *S. aureus* $\sigma^{A}_{1.1}$ suppresses the DNA binding activity of free σ^{A} and σ^{A}-RNAP holoenzyme. A Structural comparison of *S. aureus* $\sigma^{A}_{1.1}$, *E. coli* $\sigma^{70}_{1.1}$ (PDB: 4LK1), and *B. subtilis* $\sigma^{A}_{1.1}$ (PDB: 5MWW). The structure of *S. aureus* $\sigma^{A}_{1.1}$ is predicted by AlphaFold. **B** Fluorescence polarization assay shows that $\sigma^{A}_{1.1}$ truncated σ^{A} binds promoter DNA better than the full-length σ^{A}. Error bars represent mean ± SD of $n = 3$ experiments. 1.25 μM, $p = 0.0027$; 2.5 μM, $p = 0.0019$; 5 μM, $p = 0.0008$; 10 μM, $p = 0.0003$. Two-tailed Student's t test. Source data are provided as a Source Data file. **C** EMSA shows that truncation of $\sigma^{A}_{1.1}$ increases σ^{A}-dependent RPo formation. Source data are provided as a Source Data file.

buffer B. The column was washed with 25 mL buffer B containing 20 mM imidazole and eluted with 25 mL buffer B containing 0.3 M imidazole. The eluate was further purified by anion-exchange chromatography on a HiTrap Q HP column (GE Healthcare, Inc.). Fractions containing *S. aureus* σ^{A} and σ^{B} were applied to a HiLoad 16/600 Superdex 200 column (GE Healthcare, Inc.) equilibrated in 10 mM HEPES, pH 7.5, and 100 mM KCl, and the column was eluted with 120 mL of the same buffer. Fractions containing *S. aureus* σ^{A} and σ^{B} were stored at −80 °C. Yields were ~3 mg/L. Mutant proteins were purified in the same way as wild-type protein.

Expression and purification of *S. aureus* RNAP holoenzyme

S. aureus RNAP core enzyme and *S. aureus* σ were incubated in a 1:4 ratio for 1 h at 4 °C. The reaction mixtures were applied to a Superose 6 column (GE Healthcare, Inc.) equilibrated in 10 mM HEPES, pH 7.5, and 100 mM KCl, and the column was eluted with 24 mL of the same buffer. Fractions containing *S. aureus* RNAP holoenzyme were stored at −80 °C.

Primer extension transcription assay

5′ 6-FAM labeled RNA and template strand DNA (Supplementary Data 1) were annealed at a 1:1 ratio in 50 mM Tris-HCl, pH 8.0, 0.1 M KCl, and 10 mM $MgCl_2$. Primer extension transcription assay was performed in reaction mixtures (20 μl) containing 1.2 μM hybrid, 1 μM *S. aureus* RNAP, 50 mM Tris-HCl, pH 8.0, 0.1 M KCl, and 10 mM $MgCl_2$. Reaction mixtures were incubated for 15 min at 25 °C, supplemented with 1.3 μM nontemplate strand DNA. After 15 min at 25 °C, 1 mM ATP and 1 mM GTP were added. Primer extension was allowed to proceed for 15 min at 37 °C. Reactions were terminated by adding 20 μl loading buffer (10 mM EDTA, 0.02% bromopheniol blue, 0.02% xylene cyanol, and 8 M urea) and boiling for 2 min. Products were applied to 15% urea-polyacrylamide slab gels (19:1 acrylamide/bisacrylamide), electrophoresed in 90 mM Tris-borate (pH 8.0) and 0.2 mM EDTA, and analyzed by Typhoon (GE Healthcare, Inc.).

Run-off transcription assay

Nontemplate strand DNA and template strand DNA (Supplementary Data 1) were annealed at a 1:1 ratio in 50 mM Tris-HCl, pH 8.0, 0.1 M KCl, and 10 mM $MgCl_2$. Run-off transcription assay was performed in reaction mixtures (10 μl) containing 5 nM DNA, 100 nM *S. aureus* RNAP holoenzyme, 50 mM Tris-HCl, pH 8.0, 0.1 M KCl, and 10 mM $MgCl_2$. Reaction mixtures were incubated for 10 min at 37 °C, supplemented with 0.2 mM CTP, 0.2 mM UTP, 0.2 mM GTP, and 0.2 μl 3.3 μM [α-^{32}P] ATP (100 Bq/fmol). RNA synthesis was allowed to proceed for 10 min at 37 °C. Reactions were terminated by adding 10 μl loading buffer (10 mM EDTA, 0.02% bromopheniol blue, 0.02% xylene cyanol, and 8 M urea) and boiling for 2 min. Products were applied to 15% urea-polyacrylamide slab gels (19:1 acrylamide/bisacrylamide), electrophoresed in 90 mM Tris-borate (pH 8.0) and 0.2 mM EDTA, and analyzed by storage-phosphor scanning.

Ribogreen transcription assay

DNA fragments corresponding to −55 to −1 of *S. aureus rrnB* P1 and *yabJ* promoters followed by 311 bp random sequence and tR2 terminator (Supplementary Data 1) were synthesized and inserted into a pUC vector (Genewiz, Inc.). The DNA fragments were amplified by PCR and purified using the QIAquick PCR Purification Kit (Qiagen, Inc.). Ribogreen transcription assay was performed in 96-well flat-bottom black microplates. Reaction mixtures (20 μL) contained 20 nM DNA, 100 nM *S. aureus* RNAP holoenzyme, 1 mM NTPs, 50 mM Tris-HCl, pH 8.0, 0.1 M KCl, and 10 mM $MgCl_2$. Reaction mixtures were incubated for 60 min at 37 °C, supplemented with 1 μL of 5 mM $CaCl_2$ and 1 μL of DNase I (ThermoFisher, Inc.). DNA digestion was allowed to proceed for 90 min at 37 °C. Reactions were terminated by adding 1:500 diluted ribogreen (Invitrogen, Inc.) in 100 μL TE buffer (10 mM Tris-HCl, pH 8.0, 1 mM EDTA). Fluorescence emission intensities were measured using a Varioskan Flash Multimode Reader (ThermoFisher, Inc.; excitation wavelength = 485 nm; emission wavelength = 528 nm).

Fluorescence polarization assay

3′ 6-FAM labeled template strand DNA and unmodified nontemplate strand DNA (Supplementary Data 1) were annealed at a 1:1 ratio in 50 mM Tris-HCl, pH 8.0, 0.1 M KCl, and 10 mM $MgCl_2$. Equilibrium fluorescence polarization assays were performed in a 96-well microplate format. Reaction mixtures (100 μl) contained: 0–10 μM σ^{A} or σ^{A} derivative, 0.1 μM 6-FAM-labeled DNA scaffold, 50 mM Tris-HCl, pH 8.0, 0.1 M KCl, and 10 mM $MgCl_2$. Following incubation mixtures for 10 min at 25 °C, fluorescence emission intensities were measured using a BioTek Synergy H1 microplate reader (Agilent, Inc.; excitation wavelength = 485 nm; emission wavelength = 525 nm). Fluorescence polarization was calculated using:

$$P = (I_{VV} - I_{VH})/(I_{VV} + I_{VH}) \quad (1)$$

where I_{VV} and I_{VH} are fluorescence intensities with the excitation polarizer at the vertical position and the emission polarizer at, respectively, the vertical position and the horizontal position.

Electrophoretic mobility shift assay

Electrophoretic mobility shift assay was performed using the same DNA fragments as ribogreen transcription assay. Reaction mixtures

https://doi.org/10.1038/s41467-024-49229-6

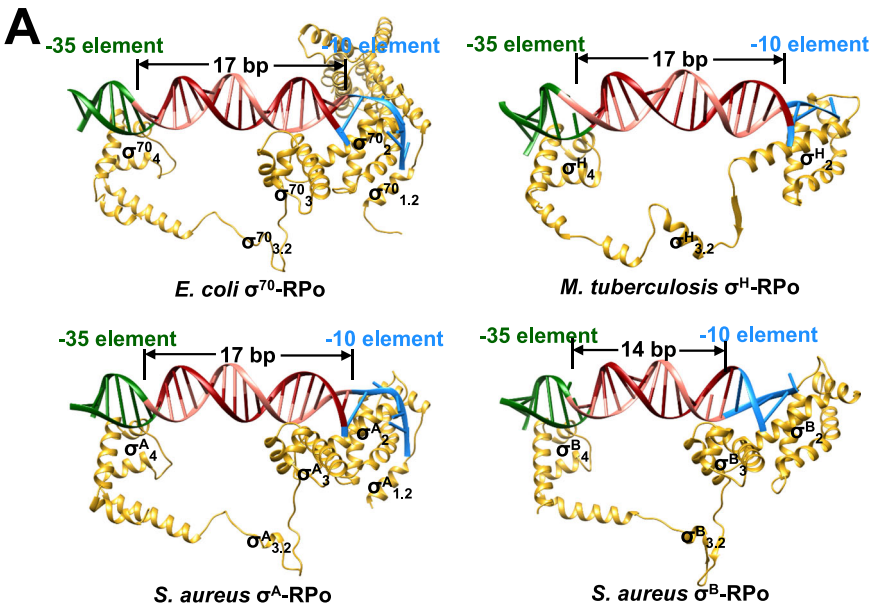

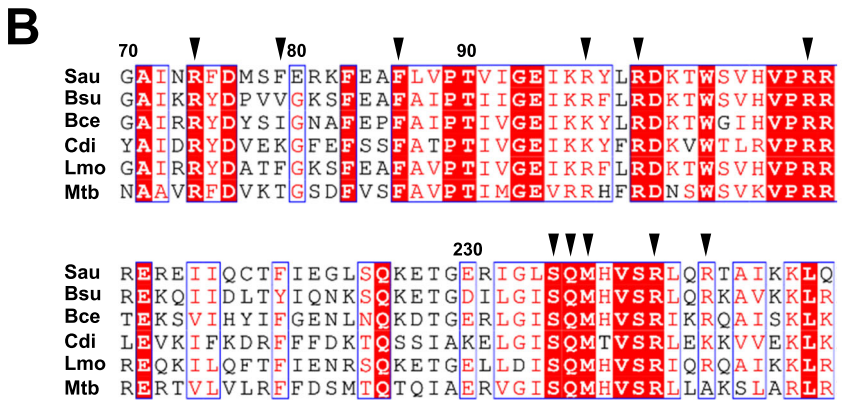

Fig. 5 | Structural comparison of *E. coli* σ^{70}-RPo, *M. tuberculosis* σ^{H}-RPo, *S. aureus* σ^{A}-RPo, and σ^{B}-RPo. A σ-DNA interactions in *E. coli* σ^{70}-RPo (PDB: 6CA0), *M. tuberculosis* σ^{H}-RPo (PDB: 5ZX2), *S. aureus* σ^{A}-RPo, and σ^{B}-RPo. Yellow, σ; salmon, nontemplate strand DNA; red, template strand DNA; green, −35 element; blue, −10 element. **B** Sequence alignment of σ^{B} orthologs from *S. aureus* (Sau), *Bacillus subtilis* (Bsu), *Bacillus cereus* (Bce), *Clostridium difficile* (Cdi), *Listeria monocytogenes* (Lmo), and *Mycobacterium tuberculosis* (Mtb). The DNA interacting residues of *S. aureus* σ^{B} are indicated by black triangles.

(20 µL) contained 40 nM DNA, 100 nM *S. aureus* RNAP holoenzyme, 50 mM Tris-HCl, pH 8.0, 0.1 M KCl, and 10 mM $MgCl_2$. Reaction mixtures were incubated for 10 min at 37 °C. The reaction mixtures were applied to 5% polyacrylamide slab gels (29:1 acrylamide/bisacrylamide), electrophoresed in 90 mM Tris-borate, pH 8.0, and 0.2 mM EDTA, stained with 4 S Red Plus Nucleic Acid Stain (Sangon Biotech, Inc.).

Cryo-EM grid preparation

Template strand DNA and non-template strand DNA (Genewiz, Inc.) were annealed at a 1:1 ratio in 10 mM HEPES, pH 7.5, 0.1 M KCl. Reaction mixtures (20 µL) contained 1.2 µM DNA scaffold, 1 µM *S. aureus* RNAP holoenzyme, 10 mM HEPES, pH 7.5, 0.1 M KCl. Reaction mixtures were incubated for 10 min at 37 °C. Quantifoil grids (R 1.2/1.3, Cu, 300) were glow-discharged for 120 s at 25 mA prior to the application of 3 µL of the samples, then plunge-frozen in liquid ethane using a Vitrobot (FEI, Inc.) with 95% chamber humidity at 10 °C.

Cryo-EM data acquisition and processing

The grids were imaged using a 300 kV Titan Krios equipped with a Falcon 4 direct electron detector (FEI, Inc.). Images were recorded with EPU in counting mode with a physical pixel size of 1.19 Å and a defocus range of 1.0-2.0 µm. Images were recorded with a 7.36 s exposure to give a total dose of 51 e/Å^2. Subframes were aligned and summed using RELION's own implementation of the UCSF MotionCor2[50]. The contrast transfer function was estimated for each summed image using CTFFIND4[51]. From the summed images, approximately 1000 particles were manually picked and subjected to 2D classification in RELION[52]. 2D averages of the best classes were used as templates for auto-picking in RELION. Auto-picked particles were manually inspected, then subjected to 2D classification in RELION. Poorly populated classes were removed. The remaining particles were 3D classified in RELION using a map of *E. coli* TEC (EMD-8585 [https://www.ebi.ac.uk/pdbe/entry/emdb/EMD-8585])[53] low-pass filtered to 40 Å resolution as a ref. 3.D classification resulted in 4 classes, among which only one class has a clear density for RNAP. Particles in this class were 3D auto-refined. CTF refinement and particle polishing were performed before final 3D refinement and postprocessing.

Cryo-EM model building and refinement

The models of *S. aureus* α, β, β′, ω, δ, ε, σ^{A}, and σ^{B} predicted by AlphaFold[54] were fitted into the cryo-EM density map using Chimera[55] and were adjusted in Coot[56]. The models of DNA scaffolds were built manually in Coot. The coordinates were real-space refined with secondary structure restraints in Phenix[57].

Statistics and reproducibility

Statistics were performed in GraphPad Prism 8.0.2. No statistical method was used to predetermine sample size. No data were excluded from the analyses. The experiments were not randomized.

Reporting summary

Further information on research design is available in the Nature Portfolio Reporting Summary linked to this article.

Data availability

The cryo-EM density maps generated in this study have been deposited in the Electron Microscopy Data Bank under accession codes EMD-38087 and EMD-38088. The atomic models generated in this study have been deposited in the Protein Data Bank under accession codes 8X6F and 8X6G. The cryo-EM density map used in this study is available in the Electron Microscopy Data Bank under accession code EMD-8585. The atomic models used in this study are available in the Protein Data Bank under accession codes 4LK1, 5MWW, 5ZX2, and 6CA0. Source data are provided with this paper.

References

1. Zhang, G. et al. Crystal structure of Thermus aquaticus core RNA polymerase at 3.3 A resolution. *Cell* **98**, 811–824 (1999).
2. Chakraborty, A. et al. Opening and closing of the bacterial RNA polymerase clamp. *Science* **337**, 591–595 (2012).
3. Feklistov, A. et al. RNA polymerase motions during promoter melting. *Science* **356**, 863–866 (2017).
4. Boyaci, H., Chen, J., Jansen, R., Darst, S. A. & Campbell, E. A. Structures of an RNA polymerase promoter melting intermediate elucidate DNA unwinding. *Nature* **565**, 382–385 (2019).
5. Feklistov, A., Sharon, B. D., Darst, S. A. & Gross, C. A. Bacterial sigma factors: a historical, structural, and genomic perspective. *Annu. Rev. Microbiol.* **68**, 357–376 (2014).
6. Feklistov, A. & Darst, S. A. Structural basis for promoter-10 element recognition by the bacterial RNA polymerase sigma subunit. *Cell* **147**, 1257–1269 (2011).
7. Zhang, Y. et al. Structural basis of transcription initiation. *Science* **338**, 1076–1080 (2012).
8. Bae, B., Feklistov, A., Lass-Napiorkowska, A., Landick, R. & Darst, S. A. Structure of a bacterial RNA polymerase holoenzyme open promoter complex. *Elife* **4**, e08504 (2015).
9. Hubin, E. A. et al. Structure and function of the mycobacterial transcription initiation complex with the essential regulator RbpA. *Elife* **6**, e22520 (2017).
10. Narayanan, A. et al. Cryo-EM structure of Escherichia coli sigma70 RNA polymerase and promoter DNA complex revealed a role of sigma non-conserved region during the open complex formation. *J. Biol. Chem.* **293**, 7367–7375 (2018).
11. Forrellad, M. A. et al. Virulence factors of the Mycobacterium tuberculosis complex. *Virulence* **4**, 3–66 (2013).
12. Li, L., Fang, C., Zhuang, N., Wang, T. & Zhang, Y. Structural basis for transcription initiation by bacterial ECF sigma factors. *Nat. Commun.* **10**, 1153 (2019).
13. Danson, A. E., Jovanovic, M., Buck, M. & Zhang, X. Mechanisms of sigma54-dependent transcription initiation and regulation. *J. Mol. Biol.* **431**, 3960–3974 (2019).
14. Yang, Y. et al. Structures of the RNA polymerase-sigma54 reveal new and conserved regulatory strategies. *Science* **349**, 882–885 (2015).
15. Glyde, R. et al. Structures of bacterial RNA polymerase complexes reveal the mechanism of DNA loading and transcription initiation. *Mol. Cell* **70**, 1111–1120 (2018).
16. Campbell, E. A., Kamath, S., Rajashankar, K. R., Wu, M. & Darst, S. A. Crystal structure of Aquifex aeolicus sigmaN bound to promoter DNA and the structure of sigmaN-holoenzyme. *Proc. Natl. Acad. Sci. USA* **114**, E1805–E1814 (2017).
17. Mueller, A. U. et al. A general mechanism for transcription bubble nucleation in bacteria. *Proc. Natl. Acad. Sci. USA* **120**, e2220874120 (2023).
18. Haldenwang, W. G. & Losick, R. A modified RNA polymerase transcribes a cloned gene under sporulation control in Bacillus subtilis. *Nature* **282**, 256–260 (1979).
19. Giachino, P., Engelmann, S. & Bischoff, M. SigmaB activity depends on RsbU in Staphylococcus aureus. *J. Bacteriol.* **183**, 1843–1852 (2001).
20. Palma, M. & Cheung, A. L. sigmaB activity in Staphylococcus aureus is controlled by RsbU and an additional factor(s) during bacterial growth. *Infect. Immun.* **69**, 7858–7865 (2001).
21. Bischoff, M. et al. Microarray-based analysis of the Staphylococcus aureus sigmaB regulon. *J. Bacteriol.* **186**, 4085–4099 (2004).
22. Jenul, C. & Horswill, A. R. Regulation of Staphylococcus aureus virulence. *Microbiol. Spectr.* **7**, GPP3-0031-2018 (2019).
23. Cheung, G. Y. C., Bae, J. S. & Otto, M. Pathogenicity and virulence of Staphylococcus aureus. *Virulence* **12**, 547–569 (2021).
24. Murakami, K. S. X-ray crystal structure of Escherichia coli RNA polymerase sigma70 holoenzyme. *J. Biol. Chem.* **288**, 9126–9134 (2013).
25. Lin, W. et al. Structural basis of Mycobacterium tuberculosis transcription and transcription inhibition. *Mol. Cell* **66**, 169–179 (2017).
26. Shen, L. et al. An SI3-sigma arch stabilizes cyanobacteria transcription initiation complex. *Proc. Natl. Acad. Sci. USA* **120**, e2219290120 (2023).
27. Cao, X. et al. Basis of narrow-spectrum activity of fidaxomicin on Clostridioides difficile. *Nature* **604**, 541–545 (2022).
28. Newing, T. P. et al. Molecular basis for RNA polymerase-dependent transcription complex recycling by the helicase-like motor protein HelD. *Nat. Commun.* **11**, 6420 (2020).
29. Pei, H. H. et al. The delta subunit and NTPase HelD institute a two-pronged mechanism for RNA polymerase recycling. *Nat. Commun.* **11**, 6418 (2020).
30. Chen, J. et al. Stepwise promoter melting by bacterial RNA polymerase. *Mol. Cell* **78**, 275–288 (2020).
31. Shin, Y. et al. Structural basis of ribosomal RNA transcription regulation. *Nat. Commun.* **12**, 528 (2021).
32. He, D. et al. Pseudomonas aeruginosa SutA wedges RNAP lobe domain open to facilitate promoter DNA unwinding. *Nat. Commun.* **13**, 4204 (2022).
33. Lin, Z., Wang, F., Shang, Z. & Lin, W. Biochemical and structural analyses reveal critical residues in delta subunit affecting its bindings to beta' subunit of Staphylococcus aureus RNA polymerase. *Biochem. Biophys. Res. Commun.* **545**, 98–104 (2021).
34. Weiss, A., Ibarra, J. A., Paoletti, J., Carroll, R. K. & Shaw, L. N. The delta subunit of RNA polymerase guides promoter selectivity and virulence in Staphylococcus aureus. *Infect. Immun.* **82**, 1424–1435 (2014).
35. Dombroski, A. J., Walter, W. A., Record, M. T. Jr., Siegele, D. A. & Gross, C. A. Polypeptides containing highly conserved regions of transcription initiation factor sigma 70 exhibit specificity of binding to promoter DNA. *Cell* **70**, 501–512 (1992).
36. Bae, B. et al. Phage T7 Gp2 inhibition of Escherichia coli RNA polymerase involves misappropriation of sigma70 domain 1.1. *Proc. Natl. Acad. Sci. USA* **110**, 19772–19777 (2013).
37. Mekler, V. et al. Structural organization of bacterial RNA polymerase holoenzyme and the RNA polymerase-promoter open complex. *Cell* **108**, 599–614 (2002).
38. Zachrdla, M. et al. Solution structure of domain 1.1 of the sigmaA factor from Bacillus subtilis is preformed for binding to the RNA polymerase core. *J. Biol. Chem.* **292**, 11610–11617 (2017).

39. Saecker, R. M. et al. Structural origins of Escherichia coli RNA polymerase open promoter complex stability. *Proc. Natl. Acad. Sci. USA* **118**, e2112877118 (2021).
40. Petersohn, A. et al. Identification of sigmaB-dependent genes in Bacillus subtilis using a promoter consensus-directed search and oligonucleotide hybridization. *J. Bacteriol.* **181**, 5718–5724 (1999).
41. van Schaik, W., Tempelaars, M. H., Wouters, J. A., de Vos, W. M. & Abee, T. The alternative sigma factor sigmaB of Bacillus cereus: response to stress and role in heat adaptation. *J. Bacteriol.* **186**, 316–325 (2004).
42. Kint, N. et al. The alternative sigma factor sigma(B) plays a crucial role in adaptive strategies of Clostridium difficile during gut infection. *Environ. Microbiol.* **19**, 1933–1958 (2017).
43. Kazmierczak, M. J., Mithoe, S. C., Boor, K. J. & Wiedmann, M. Listeria monocytogenes sigma B regulates stress response and virulence functions. *J. Bacteriol.* **185**, 5722–5734 (2003).
44. Beaucher, J. et al. Novel anti-σ factor antagonists control σF activity by distinct mechanisms. *Mol. Microb.* **45**, 1527–1540 (2002).
45. Lopez de Saro, F. J., Yoshikawa, N. & Helmann, J. D. Expression, abundance, and RNA polymerase binding properties of the delta factor of Bacillus subtilis. *J. Biol. Chem.* **274**, 15953–15958 (1999).
46. Hyde, E. I., Hilton, M. D. & Whiteley, H. R. Interactions of Bacillus subtilis RNA polymerase with subunits determining the specificity of initiation. *J. Biol. Chem.* **261**, 16565–16570 (1986).
47. Wiggs, J. L., Gilman, M. Z. & Chamberlin, M. J. Heterogeneity of RNA polymerase in Bacillus subtilis: evidence for an additional sigma factor in vegetative cells. *Proc. Natl. Acad. Sci. USA* **78**, 2762–2766 (1981).
48. Zimmerli, W. & Sendi, P. Role of rifampin against staphylococcal biofilm infections in vitro, in animal models, and in orthopedic-device-related infections. *Antimicrob. Agents Chemother.* **63**, e01746–01718 (2019).
49. Achermann, Y. et al. Factors associated with rifampin resistance in staphylococcal periprosthetic joint infections (PJI): a matched case-control study. *Infection* **41**, 431–437 (2013).
50. Zheng, S. Q. et al. MotionCor2: anisotropic correction of beam-induced motion for improved cryo-electron microscopy. *Nat. Methods* **14**, 331–332 (2017).
51. Rohou, A. & Grigorieff, N. CTFFIND4: fast and accurate defocus estimation from electron micrographs. *J. Struct. Biol.* **192**, 216–221 (2015).
52. Scheres, S. H. RELION: implementation of a Bayesian approach to cryo-EM structure determination. *J. Struct. Biol.* **180**, 519–530 (2012).
53. Kang, J. Y. et al. Structural basis of transcription arrest by coliphage HK022 Nun in an Escherichia coli RNA polymerase elongation complex. *Elife* **6**, e25478 (2017).
54. Jumper, J. et al. Highly accurate protein structure prediction with AlphaFold. *Nature* **596**, 583–589 (2021).
55. Pettersen, E. F. et al. UCSF Chimera–a visualization system for exploratory research and analysis. *J. Comput. Chem.* **25**, 1605–1612 (2004).
56. Emsley, P. & Cowtan, K. Coot: model-building tools for molecular graphics. *Acta Crystallogr. D Biol. Crystallogr.* **60**, 2126–2132 (2004).
57. Adams, P. D. et al. PHENIX: a comprehensive Python-based system for macromolecular structure solution. *Acta Crystallogr. D Biol. Crystallogr.* **66**, 213–221 (2010).

Acknowledgements

We thank Shenghai Chang at the Center of Cryo Electron Microscopy in Zhejiang University School of Medicine and Liangliang Kong at the cryo-EM center of the National Center for Protein Science Shanghai for help with cryo-EM data collection. We thank Cheng Ma and Li Liu from the Core Facilities, Zhejiang University School of Medicine for their technical support. This work was funded by National Key R&D Program of China (2023YFC2307100 to Y.F.), National Natural Science Foundation of China (32270030 to Y.F.).

Author contributions

L.Y., Q.L., L.X., and B.W. performed the experiments. Y.F. supervised the experiments. All authors contributed to the analysis of the data and the interpretation of the results. Y.F. wrote the manuscript with contributions from the other authors.

Competing interests

The authors declare no competing interests.

Additional information

Supplementary information The online version contains supplementary material available at https://doi.org/10.1038/s41467-024-49229-6.

Correspondence and requests for materials should be addressed to Yu Feng.

Peer review information *Nature Communications* thanks Dmitry Temiakov, Xiaodong Zhang, and the other, anonymous, reviewers for their contribution to the peer review of this work. A peer review file is available.